COMPARATIVE STUDIES OF AERODYNAMIC DRAG USING INVISCID FLOW COMPUTATION AND NEWTONIAN METHOD AT HIGH SPEED

R. C. Mehta* and S.B. Tiwari+

Abstract

The flow field analysis over various reentry configurations is studied numerically by solving time-dependent compressible Euler equations. The governing fluid flow equations are discretized in spatial coordinates employing a finite volume approach, which reduces the equations to semi-discretized ordinary differential equations. Temporal integration is performed using multi-stage Runge-Kutta time stepping scheme. A local time step is used to achieve steady state solution. The numerical computation is carried out for freestream Mach number of 10.0 and angle of attack of 10.0 degree. The flow features around the blunt body are characterized by a bow shock wave, expansion wave and base flow region. The numerical scheme captures all the flow field features well. Comparisons of the flow field and surface pressure distribution results are made between different configurations of the blunt body capsules such as ARD (ESA' s Atmospheric Reentry Demonstrator), Apollo II, MUSES-C, OREX (Orbital Reentry Experiments) with and without shoulder curvature and spherically blunted cone with flare angle of 30 and 35 degree. The inviscid analysis takes into consideration centrifugal force and expansion fan at the shoulder of the reentry capsules. The effects of the capsule geometry on the flow field may be useful for optimization of the reentry capsule. The Newtonian flow assumptions are used to calculate forebody aerodynamic drag for various blunt- bodies in conjunction with the NISA software. A comparison between CFD and the Newtonian flow assumptions for various reentry modules are made, and comparison shows an agreement between them.

Introduction

A high-speed flow past a blunt body generates a bow shock wave, which causes a rather high surface pressure, and as a result the development of high aerodynamic drag which is needed for aerobraking. Blunt body has been proposed as an efficient way to decelerating spacecraft for space research. Most current aerobrake designs feature a blunt fore body shielding the payload from the intense heat generated during atmospheric re-entry. The features of flow field over the blunt body capsule can be delineated through the experimental investigations at high speeds that can be described by following and also depicted in Fig. 1. In the fore body region the fluid rapidly decelerates through the bow shock wave, which causes high pressure, temperature and density depending upon the speed and altitude of the returning capsule. At the shoulder, the flow turns and expands rapidly, and boundary layer detaches, forming a free shear layer that separates the inner recirculating region behind the base flow from the outer flow field. The latter is recompressed and turned back to free stream direction, first by the so-called slip flow, and further downstream by recompression shock. At the end of the recirculation past the neck, the shear layer develops in the wake trail. A complex inviscid wave structure often includes a lip shock (associates with the comer expansion) and a wake shock (adjacent to the shear layer confluence). The corner expansion process is a modified Prandtl-Mayer pattern distorted by the presence of the approaching boundary layer. As the flow breaks away from the base plane it is brought to the base pressure by a weak shock wave known as the 'lip shock' downstream from the lip shock the free shear layer begins to form. A free shear layer (in contrast to a boundary layer) is characterized by nearly zero velocity derivatives (shear stresses) at each edge of the layer. The bow shock wave is detached from the blunt forebody and is having a mixed subsonic-super-

---

* Aerodynamics Division, Vikram Sarabhai Space Centre, ISRO Post, Thiruvananthapuram-695 022, India
Presently Professor, Department of Aeronautical Engineering, Noor Islam College of Engineering, Kumaracoil, Thuckalay-629 175
Email : atulm@md4.vsnl.net.in
+ Structural Design and Analysis Division, Vikram Sarabhai Space Centre, ISRO Post, Thiruvananthapuram-695 022, India
Manuscript received on 31 Mar 2007; Paper reviewed, revised, re-revised and accepted on 05 Dec 2007

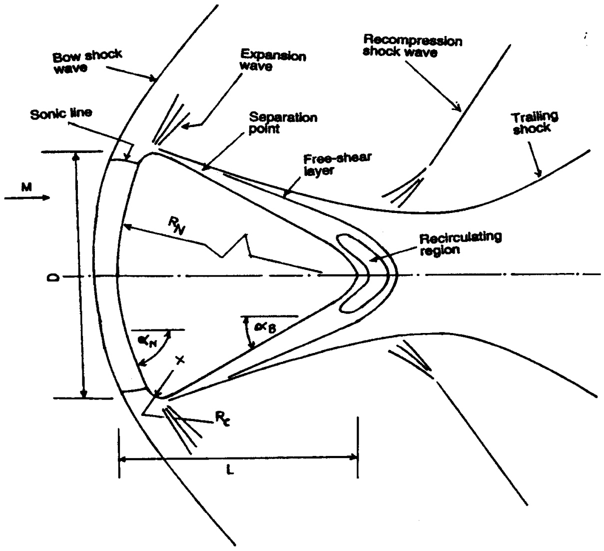

Fig.1 Representation of flow features on the blunt body at supersonic speeds

sonic region between them. The surface pressure distribution, the location of the sonic line and the shock stand-off distance on the spherical cap have been analytically calculated at very high speeds with an adiabatic index near to unity which gives a singular point at 60 degree from the stagnation point. In contrast to the base pressure, the relative low velocity adjacent to the base plane significantly affects the level of base plane heat convection.

Recently, a large number of numerical simulations [1-6] have been performed for aerobraking and blunt body capsules. The Navier-Stokes computations of the near wake reported by Allen and Cheng [4] regarding the mechanism of separation confirm the observation of Weinbaum [5]. Base drag represents the loss in recovery of pressure over the base of the body. A summary of developments relating to base pressure predictions is described in the review paper of Lamb and Oberkampf [6]. A COMET blunt body capsule is an axisymmetric design with a spherical heat shield of 1.22 m radius. The frontal diameter and area are 1.32 m and 1.37 m^2, respectively have been analysed using thin layer Navier-Stokes solver LAURA [7]. The geometrical detail of MUSES-C blunt body capsule is having nose radius of 50 mm, semi apex angle 45 deg, maximum diameter 100 mm, body length 50 mm and base configuration with 45 deg truncated cone [8]. A numerical simulation code has been used for super orbital blunt body flow and has been applied to the flow field prediction around the MUSES-C blunt body capsule [9].

Yamamoto et. al [10] carried out the single-degree-of-freedom wind-tunnel test for the OREX blunt body capsule and compared the result with the flight data. Numerical simulation of the OREX configuration has been carried out by Yamamoto [11] using thin layer Navier-Stokes solver. Tam [12] has used LUSGS implicit scheme for flow computation over the blunt body vehicle. The double cone configuration consists of two-different cone half-angles with an upstream 25 deg section followed by a downstream section. The Beagle blunt body is having 60 deg half angle cone with a maximum diameter of 0.9 m. It has a spherically blunted nose of radius 0.417 m and a shoulder radius of 0.029 m. The comer radius for Beagle has been chosen to match the peak heat transfer at this point with the peak stagnation point heat transfer. The back shell of Beagle is inclined to approximately 47 deg to the capsule's axis of symmetry. Mars pathfinder vehicle heating has been numerically computed [13] along with fore body and wake flow structure during atmospheric entry of the Mars pathfinder spacecraft [14] and [15]. The CARINA capsule is an Apollo-Gemini like module. The Apollo fore body is a truncated sphere with rounded corners. A truncated spherical is attached to the base line shape with a 0.195 deg cant angle measured from centre line. The supersonic and hypersonic laminar flow over a slender cone has been numerically calculated by Tai and Kao [16]. In many cases geometrical simplifications of configurations used for Computational Fluid Dynamics evaluation introduces errors in aerodynamic quantities comparable than those arising from numerical accuracy or lack of physical modeling of the respective code [16].

In the present work, numerical studies were undertaken for a freestream Mach number of 10.0 and angle of attack of 10 degree to solve three-dimensional compressible unsteady Euler equations. The numerical simulation is carried out employing three-stage Runge-Kutta time-stepping scheme. The numerical scheme is second order accurate in space and time. A local time stepping is used to achieve steady state solution. The Newtonian flow assumptions are used to calculate fore body aerodynamic drag for various blunt- bodies in conjunction with the NISA software. The objective of the present study is to compare the fore body aerodynamic drag coefficient of the CFD and the Newtonian flow assumptions for different blunt body configurations that will be helpful for preliminary design of the reentry capsules. The present work also includes the characterize the computational aspects of the problem, to compare the aerodynamic drag and to gain insight into flow field structure.

Governing Equations

The time-dependent compressible Euler equations are written as

$$\frac{\partial \mathbf{U}}{\partial t}+\frac{\partial \mathbf{F}}{\partial x}+\frac{\partial \mathbf{G}}{\partial y}+\frac{\partial \mathbf{H}}{\partial z}=0 \tag{1}$$

where

$$\mathbf{U}=\begin{bmatrix}\rho\\ \rho u\\ \rho v\\ \rho w\\ \rho e\end{bmatrix},\ \mathbf{F}=\begin{bmatrix}\rho u\\ \rho u^2+p\\ \rho u v\\ \rho u w\\ (\rho e+p)u\end{bmatrix},$$

$$\mathbf{G}=\begin{bmatrix}\rho v\\ \rho uv\\ \rho v^2+p\\ \rho v w\\ (\rho e+p)v\end{bmatrix},\ \mathbf{H}=\begin{bmatrix}\rho w\\ \rho u w\\ \rho v w\\ \rho w^2+p\\ (\rho e+p)w\end{bmatrix}$$

are the **U** state vector conserved quantities with ρ, u, v, w and e denoting the density, Cartesian velocity components, and the specific total internal energy, respectively, and inviscid flux vectors, **F**, **G** and **H** in the Cartesian coordinate. With the ideal gas assumption, the pressure and total enthalpy can be expressed as

$$\rho e=\frac{p}{(\gamma-1)}+\frac{1}{2}\rho\left(u^2+v^2+w^2\right) \tag{2}$$

where γ is the ratio of specific heats. The ratio of the specific heats is calculated using Hansen table [17].

Finite Volume Method

Equation (1) can be written in the integral form over a finite volume fixed in time as

$$\frac{\partial}{\partial t}\int_{\Omega}\mathbf{U}\,d\Omega+\int_{S}(\mathbf{F}+\mathbf{G}+\mathbf{H})\,\vec{n}\,dS=0 \tag{3}$$

where Ω is the arbitrary control volume with the closed boundary $\partial\Omega$ and S is the control surface, and n is the outward normal facing unit vector. The state variables **U** are volume-averaged values. A finite volume cell is specified by eight comers, which are connected by straight lines. The discrete values of the flow quantities are calculated at the centre of the cell. The surface integral of Eq. (3) over the convective part of the flux density tensor is evaluated for each component cell using an arithmetic average of the flux quantities at the vertices to determine the values on each of the cell faces. Then, the resultant convective inflow of mass, momentum, energy associated with point (i, j, k) is computed by summing the contributions of the component cells. Any open-surface element for a given boundary has a unique, effective surface vector **S** that is independent of the shape of the surface. This is because, by applying the divergence theorem to a constant vector, the integral of the outward-oriented surface normal over a closed surface vanishes. Fig.2 shows hexahedral cell in the computational domain. For instance, the surface vector $\mathbf{S}_{5678}$ is independent of the choice of which partitioning surface diagonal is used to define the cell volume with vertices 1 to 8. Whether the four vertices are on a plane or not, the surface vector is equal to one-half the cross product of its diagonal line segment. Given eight arbitrary comer points prescribing a general hexahedral, a simple way to define a shape whose volume can be precisely calculated is to partition each face into two planar triangles. The volume is then dependent on which diagonal is used on each face. The volume is the dependent on which diagonal is based on each face, since the diagonal of four non-planar points do not intersect. Kordulla and Vinokur method [18] had been used here to calculate cell volume. A system of ordinary differential equations can be obtained by applying Eq. (3) to cells formed by six surfaces as

$$\Omega_{i,j,k}\frac{d\,\mathbf{U}_{i,j,k}}{dt}+\mathbf{Q}_{i,j,k}=0 \tag{4}$$

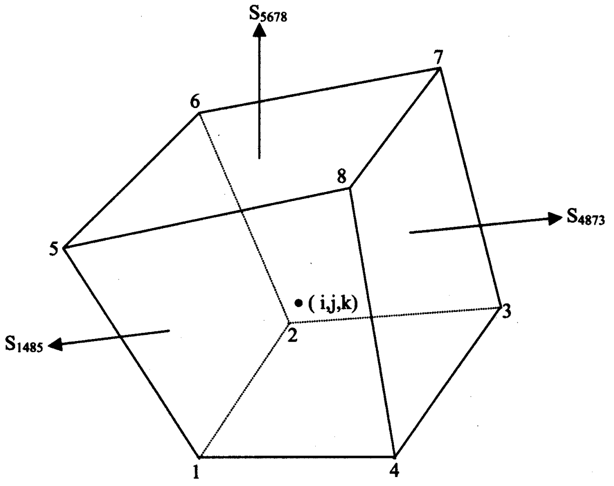

Fig.2 A hexahedral cell

where $\Omega_{i,j,k}$ is the volume of the hexahedral cell, $\mathbf{Q}_{i,j,k}$ is the convective fluxes out of the cell. The summation of the flux vectors over the six faces of the hexahedral cell is done using the average flux on each face. The above scheme reduces the centre differences scheme. It will permit nodes with odd and even decoupling.

Artificial Dissipation

In order to prevent odd-even point decoupling and oscillations near shock waves, and to obtain rapid convergence to the steady state, artificial dissipative terms, $\mathbf{D}_{i,j}$ are added to the discrete Eq. (4). The artificial dissipation model considered in this paper is based on the work of Jameson, Schmidt, and Turkel [19]. A blend of fourth and second differences is used to provide third-order background dissipation at shock waves, and is given by

$$D_{i,j\,k} = (D_x + D_y + D_z)\, U_{i,j,k} \tag{5}$$

and

$$D_x U_{i,j,k} = d_{i+1/2,j,k} - d_{i-1/2,j,k} \tag{6}$$

The dissipation fluxes $d_{i+1/2,j,k}$ are defined as a blending of first and third diferences

$$d_{i+1/2,j,k} = \varepsilon^{(2)}_{i-1/2,j,k}\, \Delta_x U_{i,j,k} + \varepsilon^{(4)}_{i-1/2,j,k}\, \Delta^3 x\, U_{i,j,k} \tag{7}$$

where Δ_x is the forward diference operator defined by

$$\Delta_x U_{i,j,k} = U_{i+1,j,k} - U_{i-1,j,k} \tag{8}$$

Exactly similar terms can be constructed for Δ_y and Δ_z. The adoptive coefficients defined as

$$\varepsilon^{(2)}_{i+1/2,j,k} = \kappa^{(2)} \max\left(\upsilon_{i-1/2,j,k}, \upsilon_{i,j,k}, \upsilon_{i+1,j,k}, \upsilon_{i+2,j,k}\right)$$

$$\varepsilon^{(4)}_{i+1/2,j,k} = \max\left(0, \kappa^{(4)} - \varepsilon^{2}_{i+1/2,j,k}\right) \tag{9}$$

are switched on or off by using the shock wave sensor *v*, with

$$\upsilon_{i,j,k} = \left| \frac{p_{i+1,j,k} - 2p_{i,j,k} + p_{i-1,j,k}}{p_{i+1,j,k} + 2p_{i,j,k} + p_{i-1,j,k}} \right| \tag{10}$$

In the present computation the values of $\kappa^{(2)}$ and $\kappa^{(4)}$ are constants, taken equal to 1/4 and 1/256, respectively. The dissipative operators in y and z directions are defined in a similar manner. The blend of second and fourth differences provides third-order background dissipation in smooth regions of the flow and first-order dissipation in shock waves.

Time-stepping Scheme

The above spatial discretization reduces the governing flow equations to semidiscrete ordinary differential equations, temporal integration is performed using multi-stage Runge-Kutta time-stepping scheme [19]. Suppressing the subscripts (i, j, k), the following steps are employed for the numerical integration

$$\begin{aligned}
U^{(0)} &= U^{n} \\
U^{(1)} &= U^{n} - 0.6\,\frac{\Delta t}{\Delta \Omega}\left(R^{(0)} - D^{(0)}\right) \\
U^{(2)} &= U^{n} - 0.6\,\frac{\Delta t}{\Delta \Omega}\left(R^{(1)} - D^{(0)}\right) \\
U^{(3)} &= U^{n} - \frac{\Delta t}{\Delta \Omega}\left(R^{(2)} - D^{(0)}\right) \\
U^{n+1} &= U^{(3)}
\end{aligned} \tag{11}$$

where n is the current time level, n+1 is the new time level, and residual **R** is the sum of the inviscid fluxes. In order to minimize the computation time, the expensive evaluation of the dissipation terms **D** is carried out only at the first stage, and then frozen for the subsequent stages. The numerical scheme is stable for a Courant number ≤ 2. A local time step is used to achieve steady state solution.

Initial and Boundary Conditions

Four types of boundary conditions are required for the computation of flow field, i.e., wall, inflow, outflow, and symmetric conditions. They are prescribed as follows:

At the solid wall no slip boundary condition is imposed and at the out flow boundary, the two tangential velocity components are extrapolated from the interior, while at the inflow boundary they are specified as having far field values. These five quantities provide a complete definition of the flow in the far field. For the supersonic case, the flow is fixed to the freestream values as given in Table-1 and the out flow is extrapolated from the values at the interior cells. The flow is tangent to the wall. The flow is

Table-1 : Trajectory points and initial conditions

M_∞	U_∞, m/s	P_∞, Pa	T_∞, K
10.0	3150	498	247

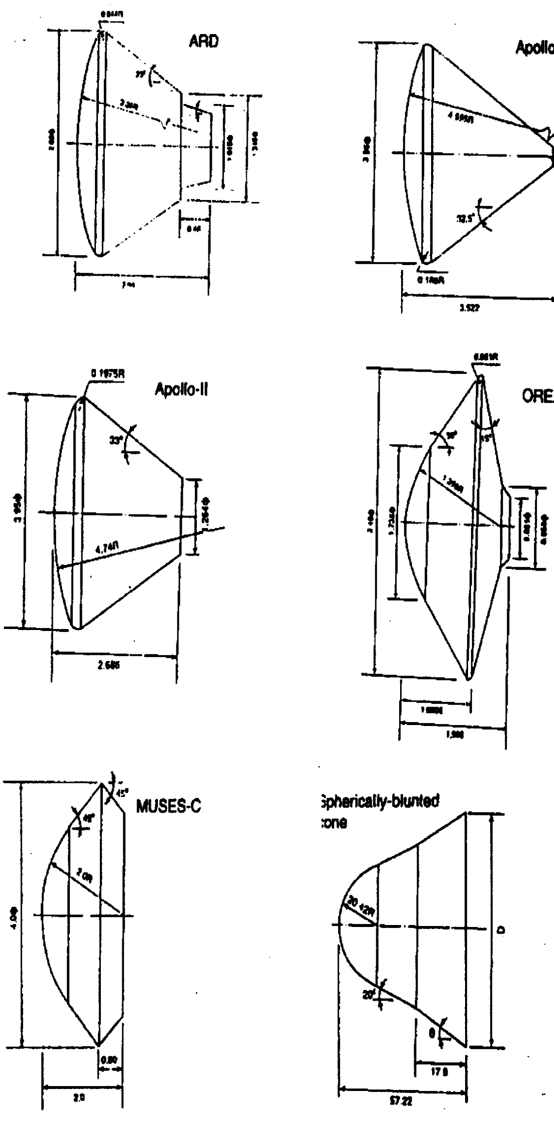

Fig.3 Geometrical detail of the blunt body

assumed to have bilateral symmetry with respect to the x-y plane, therefore w = 0, and gradients of the other primitive variables are zero on the symmetry boundary.

Reentry Capsule Configurations

The reentry capsules geometrical details are shown in Fig. 3. It can be seen from the figure that the blunt body configurations are having different shape such as spherically cap, combination of spherical cap and cone. The geometrical shape usually has chosen to meet certain design requirements such as aerodynamic load and drag. Table-2 gives the geometrical parameters of different reentry configurations.

Grid Generations

In order to initiate numerical simulation of flow over the reentry capsules, the physical space is discretized into non-uniform spaced grid points. These body-oriented grids are generated using a finite element method in conjunction with homotopy scheme [20]. The capsule computational region is divided by a number of grid points. Using these surface grid points as reference nodes, the normal coordinates is then described by stretched structured field points extending onward up to the outer computational boundary. These stretched grids are generated in an orderly manner. Grid independent tests are carried out taking into consideration the effect of the computational domain, the stretching factor to control the grid intensity near the capsule wall, the number of grid points in the axial, normal and circumferential directions. The outer boundary of the computational domain is varied from 5 to 12 times the maximum diameter, D. To validate the code, the steady state numerical computation is compared with the experimental data. This arrangement of grid is found to give a relative difference of about ±3% in the pressure peak value in the shoulder of the capsule with the convergence criterion of $|\rho^{n+1} - \rho^{n}| \leq 10^{-5}$ between two successive iterations. After extensive grid independent test, 90x42x18 grid points are taken in the longitudinal, normal and circumferential directions, respectively.

Table-2 gives the dimensional detail of the model of the blunt body configurations and also shown in Fig. 3. The surface grid is generated using NISA [21] (Numerically Integrated elements for System Analysis). The surface grids are used to compute aerodynamic load using Newtonian expression in order to compare the numerical results. Fig. 4 shows the surface grid generation over spherically blunt body with flare angle of 30 and 35 degree, ARD, Apollo II, Muses-C and OREX with and without shoulder curvature. These surface grid points are used to compute area and volume of the cell for the Newtonian flow assumptions.

Results and Discussion

The numerical procedure described in the previous sections is validated in Ref. [22]. The numerical procedure

Table-2(a) Geometrical parameters of reentry capsules

Capsule	Spherical Radius, R_N	Frontal Diameter, D	Corner Radius, R_C	Overall Length, L	Semi-cone angle, α_A deg	Back shell angle, α_B deg
ARD	3.36	2.80	0.014	2.04	-	33.0
Apollo	4.595	3.95	0.186	3.522	-	32.5
Apollo-II	4.74	3.95	0.1975	2.686	-	33.0
OREX smooth shoulder	1.35	3.40	0.001	1.508	50.0	75.0
OREX sharp shoulder	1.35	3.457	-	1.508	50.0	75.0
MUSES-C	2.0	4.0	-	2.0	45.0	45.0

Table-2(b) Geometrical parameters of spherically blunted cone blunt body

Base diameter, D	Semi-cone angle, θ
77.89	30
82.29	35

described in the previous section is applied here to compute flow field over ARD (ESA's Atmospheric Reentry Demonstrator), OREX (Orbiter Reentry Experiments) with and without smooth and a sharp shoulder edge, Apollo, and spherically blunted cone-flare with semi-cone angle, θ and 35 degree reentry modules.

Flow Characteristics

For the sake of brevity we are presenting windward and leeward sides flow field over OREX with smooth and without smooth shoulder, ARD, Apollo II and spherical-cone configurations are shown at M = 10.0 and at angle of attack 10.0 degree in Fig. 5 and corresponding variations of pressure coefficient are depicted in Fig. 6. Fig. 5 displays the flow field in the windward and the leeward side of the capsules. A shock wave stands in front of the reentry blunt body and forms a region of subsonic flow around the stagnation region. Computed Mach contour plots in the windward and the leeward side of the various capsules are shown in Fig.6 for freestream Mach number 10.0 and angle of attack 10.0 deg. Characteristic features of the flow field around the blunt body at high speed, such as bow shock wave ahead of the capsule and the expansion waves on the shoulder of the capsules. The bow shock wave follows the body contour and the fore body is entirely subsonic up to the comer tangency point of the ARD, the Apollo and the OREX where the sonic line is located. In the case of the spherically blunted cone-flare module, the sonic line is located at the junction of the sphere cone as seen in the Mach contour plots. The flow expands at the base comer. The flow field over the reentry modules became complicated due to the presence of comer at the shoulder and the base shell of the capsule as delineated in the Mach contour plots.

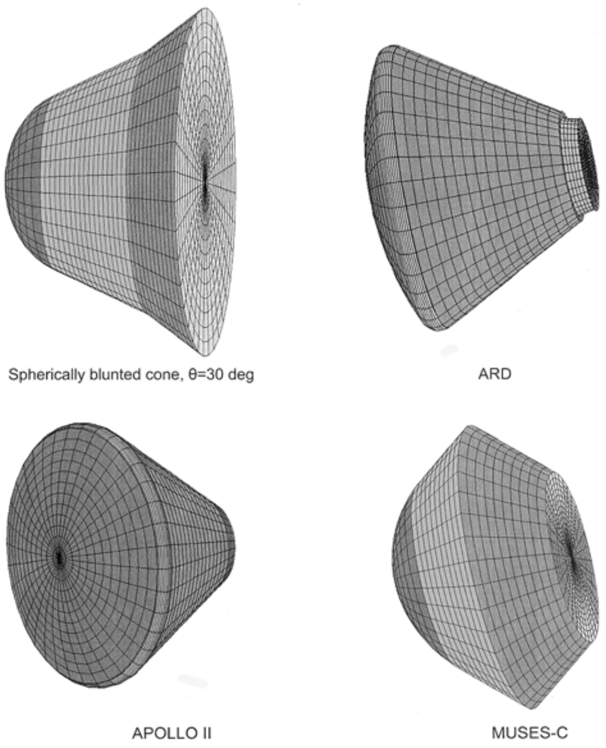

Fig.4(a) Surface grid generation over the blunt body configurations using NISA

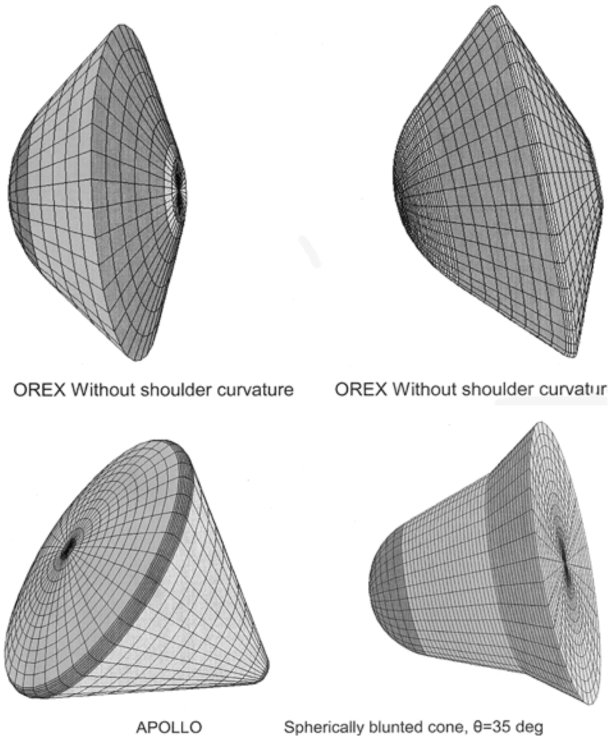

Fig.4(b) Surface grid generation over the blunt body configurations using NISA

Calculation of Aerodynamic Drag Coefficient

Pressure drag is calculated by integrating the surface pressure distribution on the fore body surface that is excluding the base of the capsule. A_{max} is the maximum cross- section area of the capsule. The fore body aerodynamic drag C_D based on the CFD analysis is given in Table-3 for ARD, Apollo II, OREX (with and without shoulder curvature) and spherically blunted cone with semi-cone angle, θ = 30 and 35 degree at free stream Mach 10 and angle of attack of 10 degree. The aerodynamic drag is greater then one for all the capsules considered in the present analysis.

Newtonian Impact Theory

In the Newtonian flow concept the shock wave is assumed to coincide with the body surface. It is also assumed that the freestream maintain its speed and direction unchanged until it strike the surface exposed to the flow. The impact theory does not specify the pressure on surface that does not "visualize" the flow, that is, the surfaces on which gas dynamics would predict Prandtl-Mayer flow. When the flow is curved in the direction of free stream, the difference in pressure from the shock wave to the body surface equals the centrifugal force, due to the curvature of the flow. The pressure coefficient [23] on the surface can be written as

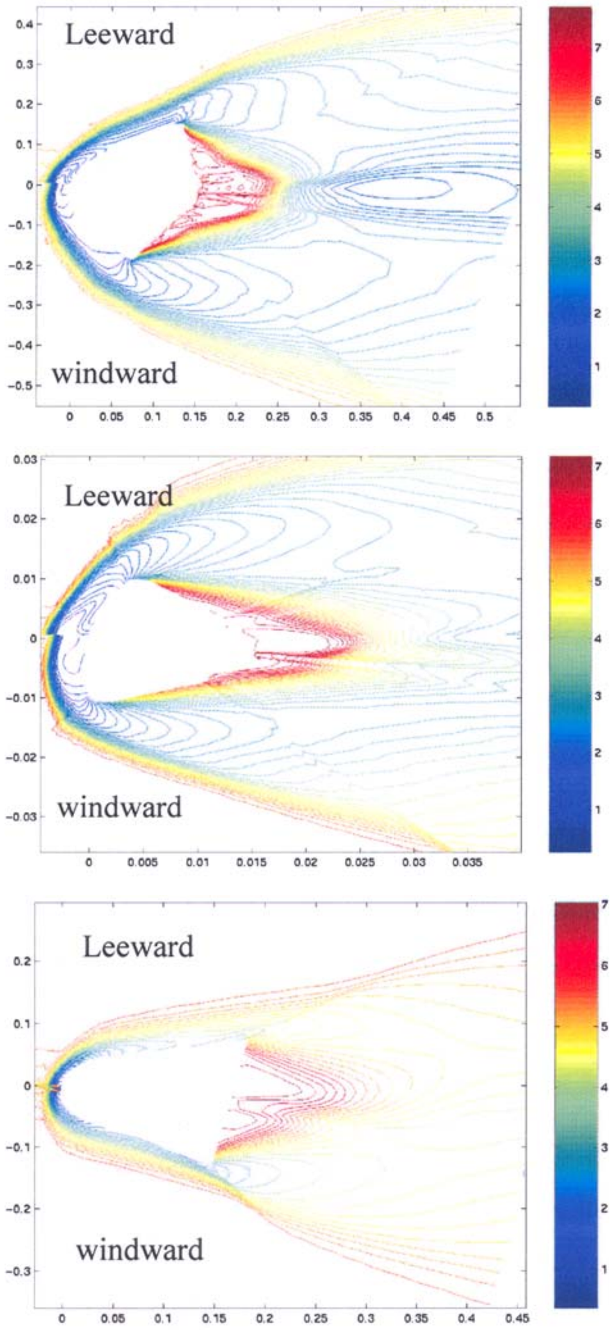

Fig.5(a) Mach contours

$$C_p = 2\cos^2\theta - \frac{2}{3}\sin^2\theta \tag{12}$$

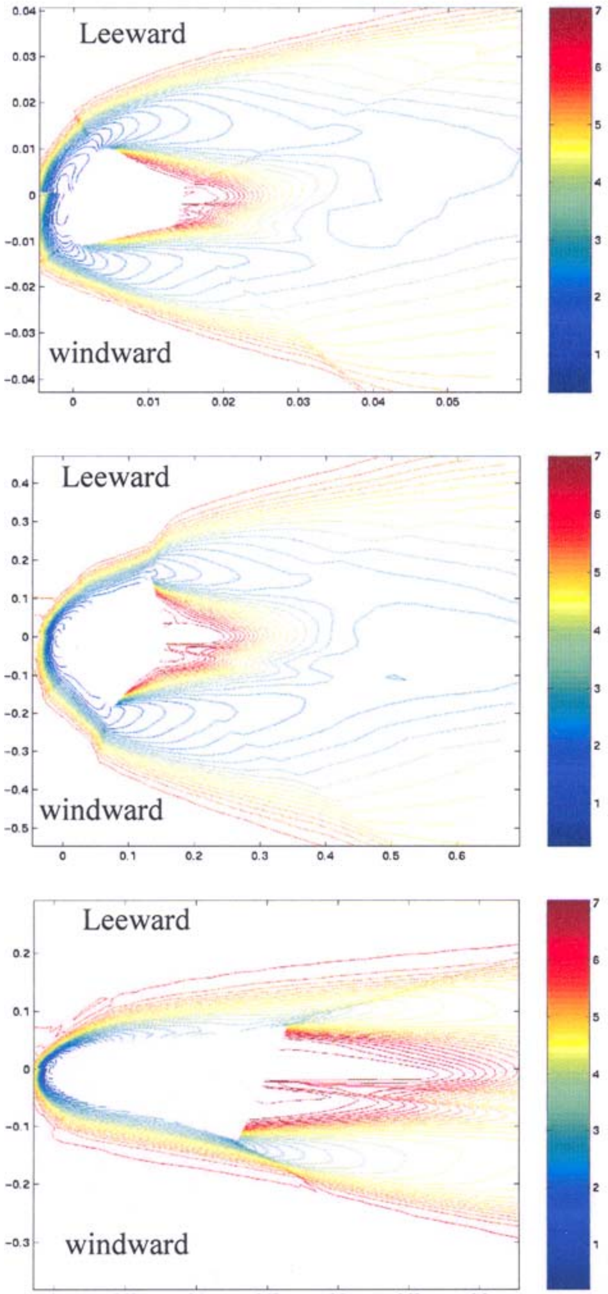

Fig.5(b) Mach contours

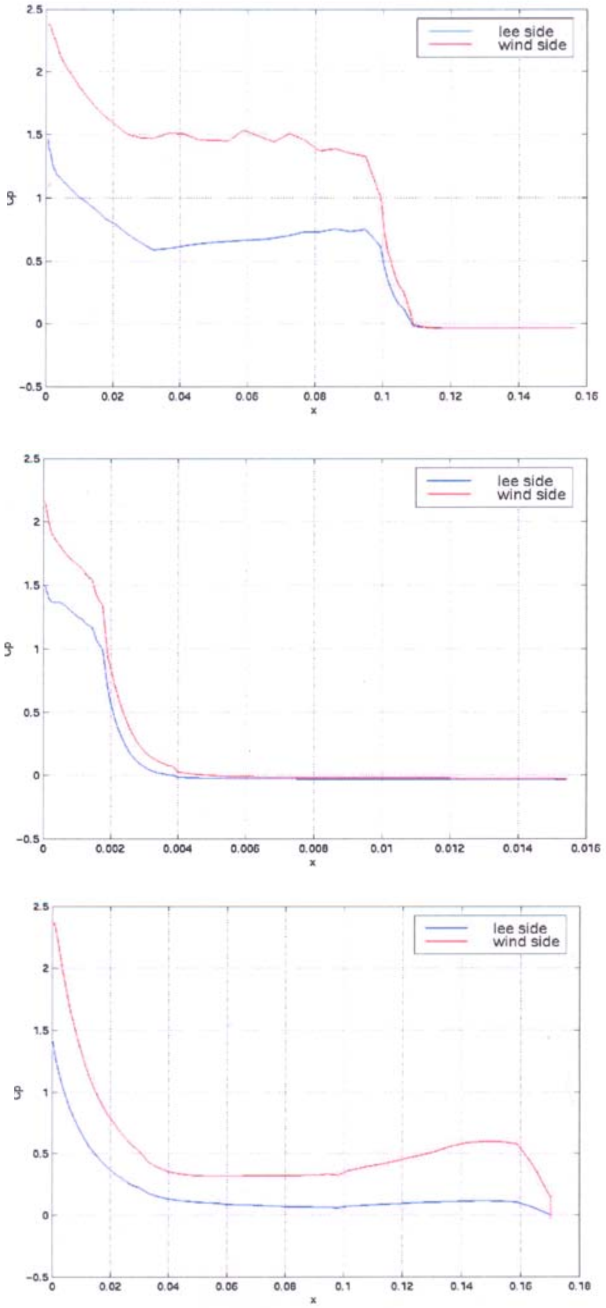

Fig.6(a) Variations pressure coefficient

where θ is the angle between the local tangent to the body surface and the freestream flow direction. The second term on the right-hand side represents the centrifugal force term. C_p equal to zero point to occur at θ = 60 deg, whereas the simple impact theory predicts it to be located at θ = 90 deg. Lees [24] proposed a modified Newtonian theory, which consists in scaling down so as to be exact at stagnation point, where is the correct value is known. The forebody aerodynamic drag is also computed using Newtonian flow assumptions.

The Newtonian flow assumptions [25] are used to calculate fore body aerodynamic drag for ARD, Apollo-II, OREX with and without shoulder curvature, MUSES-C, Apollo and spherically blunted cone with θ = 30 and 35 deg in conjunction with the NISA software. A comparison

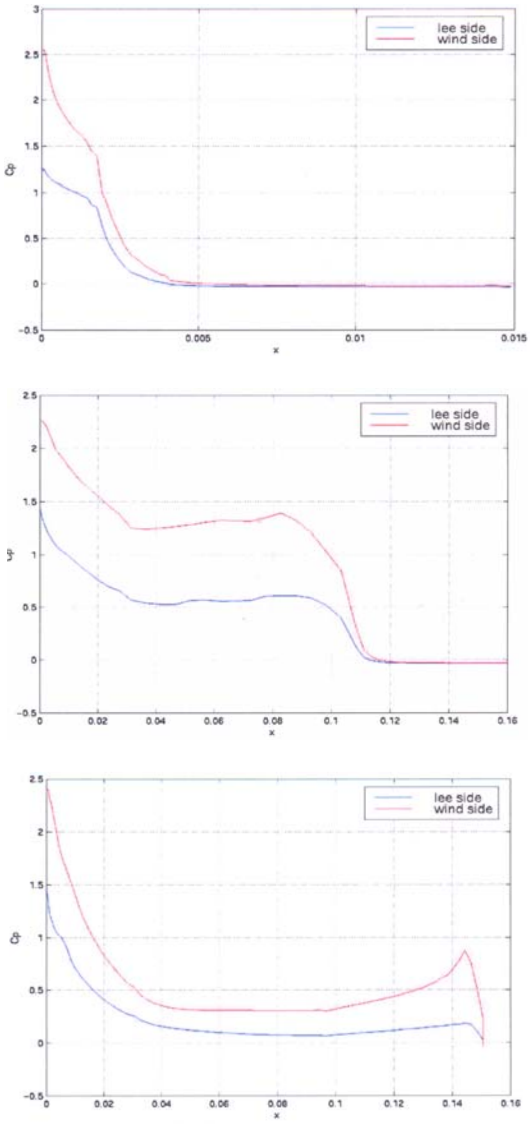

Fig.6(b) Variations pressure coefficient

between CFD and the Newtonian flow assumptions for fore body drag of ARD, Apollo II, OREX with and without shoulder curvature and spherically blunted cone configurations with θ = 30 and 35 deg are made in Table-3. The comparison shows an agreement between them.

Table-3 : Forebody aerodynamic drag

Capsule	C_D	
	CFD	Newtonian
ARD	1.44	1.48
Apollo-II	1.50	1.54
OREX-without shoulder curvature	1.12	1.15
OREX-with shoulder curvature	1.40	1.44
MUSES-C	-	1.13
Apollo	-	1.45
Spherically blunted cone, θ = 30 deg	0.38	0.35
Spherically blunted cone, θ = 35 deg	0.45	0.48

Conclusions

The flow fields over the body are simulated to solve numerically three-dimensional inviscid Euler equations. The effects of geometrical parameters, such as radius of the spherical cap, half cone angle of the forebody and flare angle of the spherically blunted cone configurations are analyzed using numerically computed results. Comparisons of the flow field and surface pressure distribution results are made between different configurations of the blunt body capsules such as ARD (ESA’ s Atmospheric Reentry Demonstrator), Apollo II, OREX (Orbital Reentry Experiments) and spherically blunted cone with semi-cone angle of 30 and 35 degree. The Newtonian flow assumptions are used to calculate fore body aerodynamic drag for various blunt-bodies in conjunction with the NISA software. A comparison is made between the CFD and the Newtonian flow assumptions for the aerodynamic drag over various blunt body configurations for freestream Mach number 10 and angle of attack of 10 degree and an agreement found between them.

Reference

1. Gnoffo, P.A., Price, J.M. and Braum, R.D., "On the Computation of Near Wake, Aerobrake Flow Fields", AlAA paper 91-1371, June 1991.

2. Grasso, F. and Marinir, M., "Solution of Hypersonic Flows with Total Variation Diminishing Multigrid Techniques", Computer and Fluids, Vol. 23, No.5, 1995, pp. 571-592.

3. Venkatapathy, E., Palmer, G. and Prabhu, D.K., "AFE Base Computations", AIAA Paper 91-1372, June 1991.

4. Allen, J.S. and Cheng, S.I., "Numerical Solution of the Compressible Navier-Stokes Equations for the

Near Wake", Physics of Fluids, Vol. 13, No.1, 1970, pp. 37-52.

5. Weinbaum, S., "Rapid Expansion of a Supersonic Boundary Layer and its Applications to the Near Wake", AlAA Journal, Vol. 4, No.2, 1966, pp. 217-226.

6. Lamb, J.P. and Oberkampf, W.L., "Review and Development of Base Pressure and Base Heating Correlations in Supersonic Flow", Journal of Spacecraft and Rockets, Vol. 32, No.1, 1995, pp. 8-23.

7. Wood, A.W., Gnoffo, P.A. and Rault, D.F.G., "Aerodynamic Analysis of Commercial Experiment Transport Blunt Body Capsule", Journal of Spacecraft and Rockets, Vol. 34, No.5, 1996, pp. 643-646.

8. Teramoto, S., Hiraki, K., and Fujii, K., "Numerical Analysis of Dynamic Stability of a Blunt Body Capsule at Transonic Speed", AIAA Journal, Vol. 39, No.4, April 2001, pp. 646-653.

9. Osu, H., Abe, T., Ohnishi, Y., Sasoh, A. and Takayama, K., "Numerical Investigation of High Enthalpy Flow Generated by Expansion Tube", AlAA Journal, Vol. 40, No. 12, 2002, pp. 2423-2430.

10. Yamamoto, Y. and Yoshioka, M., "CFD and FEM Coupling Analysis of OREX Aero-thermodynamic Flight Data", AlAA 95-2087.

11. Yamamoto, Y., Numerical Simulation of Hypersonic Viscous Flow for the Design of H-II Orbiting Plane (HOPE)", AIAA 91-1390, 1991.

12. Tam, L. T., "LU-SGS Implicit Scheme for Entry Vehicle Flow Computation and Comparison with Aerodynamic Data", AlAA 92-2671 CP, 1992.

13. Gaitonde, D.V., Canupp, P. and Holden, M.S., "Heat Transfer Predictions in Laminar Hypersonic Viscous/inviscid Interaction", Journal of Thermodynamics and Heat Transfer, Vol. 16, No.4, Oct -Dec 2002, pp. 481-499.

14. Kin, M.S., Loelbach, J.M. and Lee, K.D., "Effects of Gas Models on Hypersonic Base Flow Calculations", Journal of Spacecraft and Rockets, Vol. 31, No.2, 1994, pp. 223-230.

15. Haas, B.L. and Venkatapathy, E., "Mars Path Finder Computations Including Base Heating Predictions", AIAA 95-2086, 1995.

16. Tai, C-S. and Kao, A.F., "Navier-Stokes Solver for Hypersonic Flow Over a Slander Cone", Journal of Spacecraft and Rockets, Vol. 31, No.1, 1994, pp. 215-222.

17. Hansen, C.F., "Approximations for the Thermodynamic and Transport Properties of High Temperature air", NASA TR R-50, 1959.

18. Kordulla, W. and Vinokur, M., Efficient Computation of Volume in Flow Predictions", AIAA Journal, Vol. 21, No.6, June 1983, pp. 917-918.

19. Jameson, A., Schmidt, W. and Turkel, E., "Numerical Solution of Euler Equations by Finite Volume Methods Using Runge-Kutta time Stepping Schemes", AIAA 81-1259, 1981.

20. Mehta, R. C., "A Quasi Three Dimensional Automatic Grid Generation Method", Proceedings of the 25th National and International Conference on Fluid Dynamics and Fluid Power, Indian Institute of Technology Delhi, New Delhi, India, December, 1998, pp. 89-98.

21. NISA -II, Engineering Mechanics Research Corporation, Michigan, USA, 1994.

22. Mehta, R. C., "Flow Direction Estimation Based on Computed and Flight Measurement Surface Pressure", Computational Fluid Dynamics Journal, Vol. 12, No.3, October, 2003, pp. 555-561.

23. Truit, R. W., "Hypersonic Aerodynamics", The Ronald Press Co., New York, 1959.

24. Lees, L., "Hypersonic Flow", Institute Aeronautical Science, Preprint No. 554, 1955.

25. Wood, W. A., "Hypersonic Pitching-moment Shift for Star Dust Reentry Capsule Forebody", NASA TM 97-206266, 1997.